Materials & Design 257 (2025) 114467

Contents lists available at ScienceDirect

Materials & Design

journal homepage: www.elsevier.com/locate/matdes

Nature-inspired heterogeneous metamaterials: functional design framework

Zhuo Chen [a], Huitian Wang [a], Zihan Hu [b], Limin Zhou [b], Yiu Wing Mai [c], Robert O. Ritchie [d,*], Sha Yin [a,*]

[a] School of Aeronautic Science & Engineering, Beihang University, Beijing 100191, China
[b] Department of Automation and Intelligent Manufacturing, Southern University of Science and Technology, Shenzhen, China
[c] Department of Mechanical Engineering, The Hong Kong Polytechnic University, Kowloon, Hong Kong, China
[d] Department of Materials Science & Engineering, University of California, Berkeley, CA 94720, USA

ARTICLE INFO

Keywords:
Metamaterials
Multifunctionality
Optimization
Nature-inspired
Microstructure

ABSTRACT

Heterogeneous mechanical metamaterials can achieve extraordinary properties through their complex and diverse microstructural designs. However, research on the functional realization by heterogeneous mechanical metamaterials in varying scenarios remains insufficient. Nature's materials generally feature irregular and multi-material characteristics, endowing them with remarkable functions such as mechanical stress regulation and crush protection. Accordingly, herein, we combine these two features to create a unified framework for the design of heterogeneous mechanical metamaterials. By optimizing the spatial distribution of a limited set of unit cells, we show that irregular and multi-material metamaterials can be assembled to achieve functions such as cloak, protection, and field control characteristics, demonstrating the universality of this framework. Although our optimized structures are irregular and non-periodic, the assembled materials exhibit spatially varying characteristics, allowing precise displacement or stress distribution adjustment in different control regions under various loading conditions to achieve functionality. Our approach excels in rapidly responding to new design scenarios that offer inspiration for the efficient design of functional metamaterials.

1. Introduction

Mechanical metamaterials can achieve unique and extraordinary mechanical properties by rationalizing their microstructures [1–7]. Those with heterogeneous microstructures have gained increasing attention in recent years due to their vast design space. Specifically, reducing stress concentrations through metamaterial microstructure design can help resist structural failure [8], manipulation of stress distribution can stimulate the regeneration and repair of fractured bones [9], and optimizing microstructure distribution of multi-phase lattice materials can reduce local stress and maximize strain energy density [10–13]. Additionally, mechanical cloaks designed around objects or voids can manipulate the elastic field around them, making it difficult to distinguish the objects or voids from a uniform environment, thereby achieving mechanical "invisibility" [14–16].

To generate heterogeneous microstructures with targeted performance remains a challenging endeavor because of the infinite number of design spaces. Some pioneering approaches have been proposed, including filtered random lattices [17–19], phase-separation induced foams [20,21], biomimetic virtual growth processes [9,22,23], and data-driven design methods [24,25]. Among these, data-driven approaches are particularly powerful because they can explore the infinite design space of heterogeneous structures by leveraging extensive unit cell databases. However, in the research on data-driven design, we have found that even with an extremely diverse and complex database of microstructures, it is very difficult to effectively regulate the structural displacement field under varying scenarios. For instance, the performance of a mechanical cloak designed by data-driven methods was found to decline significantly under applied boundary forces [24]. As such, beyond pursuing complex microstructures, other potential design concepts deserve to be further examined for heterogeneous mechanical metamaterials. Also, current studies on heterogeneous mechanical metamaterials have generally focused on achieving specific functions, without validating the universality of the design methods for other various functionalities [8–10], Vangelatos et al., [24,26]. Accordingly, a universal design framework that can generate effective metamaterials

* Corresponding authors.
E-mail addresses: ritchie@berkeley.edu (R.O. Ritchie), shayin@buaa.edu.cn (S. Yin).

https://doi.org/10.1016/j.matdes.2025.114467
Received 18 April 2025; Received in revised form 26 June 2025; Accepted 24 July 2025
Available online 24 July 2025

tailored for different functional requirements remains to be fully developed.

Nature provides guiding principles for generating inherent architectures, where different parts generally exhibit various microstructures and constituting materials [27–30] (Fig. 1A), resulting in extraordinary performance [27,31–33]. The irregularity and multi-material composition of natural materials confer functional grading properties, making them highly suitable for overall functions such as fruit integrity [34], hunting and attacking [35,36], body protection [37,38], and rapid swimming [39,40]. To simulate this by mimicking their multi-material features, some remarkable results have been achieved [41–44]. Considering this, we integrated the multi-material approach with irregular structures to design heterogeneous unit cell sets, as shown in Fig. 1B (and Fig. S1 in the Supplementary Materials). Our design simplified the unit cells compared to the data-driven method and expanded the property space by varying the parent materials. Mechanical properties (*i.e.*, main diagonal components of the stiffness tensor matrix) of unit cells with different parent materials occupied different property space, shown by the gray and green illustrated areas. It is apparent that the green areas for the material of higher Young's modulus have greatly expanded the property space.

A design framework for heterogeneous mechanical metamaterials is proposed in this study, based on a constructed set of multi-material unit cells and the discontinuous variable optimization design method. This framework was designed to optimize the physical field distribution to approximate the target by setting the distribution of the corresponding physical field as optimization objectives based on the desired arbitrary functionalities. As shown in Fig. 1C, the design domain was discretized into rectangular units, with each unit number corresponding to a unique microstructure within the unit cell set. The stiffness tensor corresponding to each unit was used in a finite element calculation, with the solutions directly mapped to the final results. The metamaterial defined in this study was composed of 30 × 30 tessellated square base cells (see the Appendix in the Supplementary Materials for more details). By using the proposed heterogeneous design framework, we have achieved the development of a mechanical metamaterial with various functionalities, such as mechanical cloak, protection, shape control and field control, demonstrating the universality of the framework (Fig. 1D). Other functionalities can be obtained for any metamaterial with this design framework, extending their application in more engineering scenarios.

2. Methods

The original design domain in this study comprised a 30 × 30 grid of two-dimensional plane elements, each grid with dimensions of 5 mm × 5 mm. For finite element analysis (FEA), each element was modeled as a four-node rectangular plane element with a thickness of 10 mm. To facilitate energy-based homogenization calculations, each unit cell in the dataset was designed in a pixelated manner, represented by a 50 × 50 binary matrix. We employed a conventional genetic algorithm to optimize the filling of each unit cell. The genetic algorithm was implemented using MATLAB's built-in optimization toolbox, with default settings for selection, crossover, and mutation operations left unchanged. The algorithm terminates either when the average relative change in the best objective function value over 3000 generations falls below the specified tolerance of 1e-5, or when the maximum number of

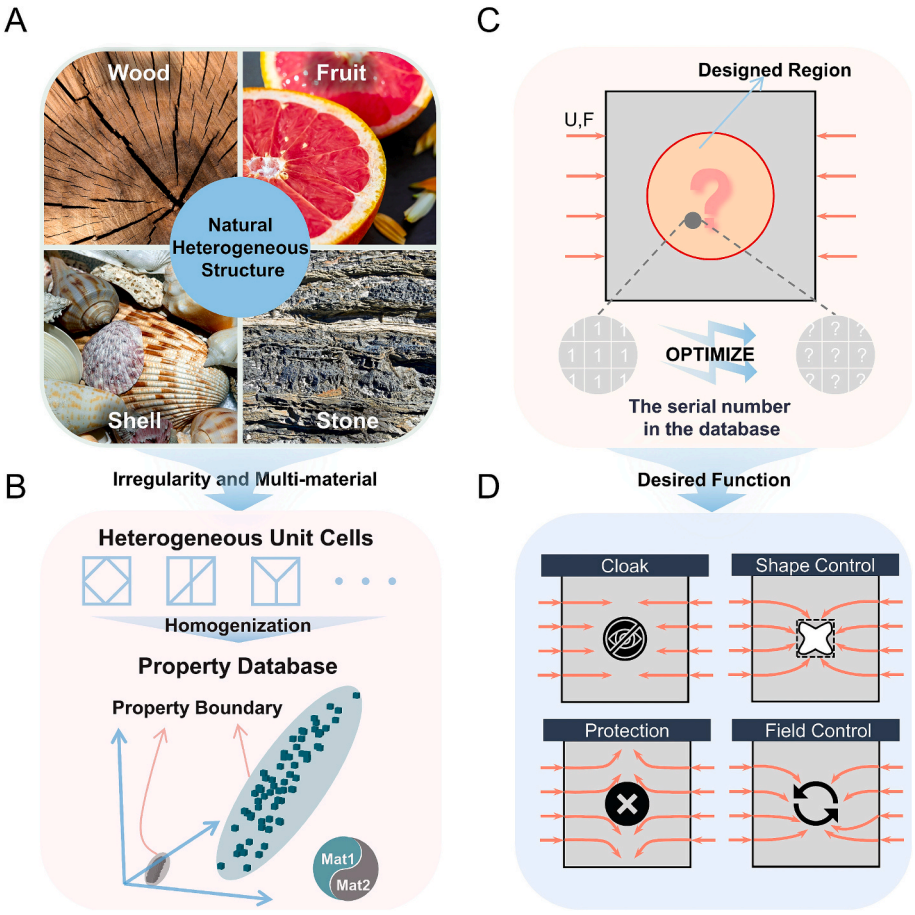

Fig. 1. Schematic diagram of the heterogeneous mechanical metamaterial design framework. (A) Naturally irregular materials found in wood, shells, stones, and fruits. (B) Construction method of unit cells and the properties space of different materials. (C) Definition and optimization of the schematic. (D) Optimized structure with the desired function.

generations, set to 30,000, is reached. Let G denote the maximum number of generations, N the population size (i.e., the number of unit cells to be optimized), and T_f the time required for the finite element analysis. In this study, the overall time complexity of the optimization is $O(G \bullet N)$. Since the finite element computations are significantly more time-consuming than the genetic operations, the total computation time can be approximated by $T_{total} \approx G \bullet N \bullet T_f$. On a single Intel(R) Xeon(R) Gold 6140 CPU, each finite element computation takes approximately 0.0345 s. Given 84 unit cells and a maximum of 30,000 iterations, the estimated total runtime is approximately 24.15 h. In practice, this time can be significantly reduced by parallelizing the computations across multiple CPUs. Because the maximal strain of the assembled structure was ~1 % to 2 %, Finite element analysis (FEA) was carried out with MATLAB and ABAQUS using linear elasticity and plane stress assumptions. The numerical calculations closely matched the measured ones, validating the effectiveness of the design framework. All the structures tested were fabricated using a Stratasys J750 Digital Anatomy 3D printer. We compressed the structures using a Zwick/Roell Z020 machine. During the experiments, the displacement field on the tested structure was captured and analyzed using a Digital Image Correlation (DIC) equipment from GOM GmbH. More details on the design methods and experiments are given in the Supplementary Information.

2.1. Database generation

This study considered anisotropic and asymmetric units, whose stiffness tensors were calculated using energy-based homogenization [45]. The base cell's homogenized elastic properties, calculated through energy-based homogenization, were$\mathbf{C}_{11}$ = 110.94 MPa, $\mathbf{C}_{12}$= 28.22 MPa, $\mathbf{C}_{22}$= 110.94 MPa, and $\mathbf{C}_{33}$ = 33.57 MPa. Inspired by multiphase lattice design, the local addition and removal of struts can introduce deliberate reinforcements and defects to modulate mechanical properties [11,12]. Accordingly, nine distinct combinations of basic strut elements were designed to introduce relative weakening and strengthening within the unit cells, resulting in a database of structures with anisotropic mechanical behavior as shown in Fig. 2A. Although more options for basic strut configurations are theoretically possible, the results of this research demonstrate that the selected nine combinations are already sufficient to achieve effective optimization outcomes. All possible combinations were generated, and duplicate structures were removed, resulting in a total of 152 unit cells. Since all unit cells include a frame, there was no need to design a new algorithm to ensure connections between the units. The struts in different directions introduced the irregularity found in natural materials, making them better suited for various loading angles and more effective at altering force transmission directions. The database is small and practical, directly applicable to discontinuous variable optimization calculations, and it significantly reduces mass production costs to some extent. Two materials with significantly different Young's modulus properties were selected. Based on ASTM standard tests, the Young's modulus and Poisson's ratio of the stiffer material were respectively 3380 MPa and 0.4, while for the other (compliant) material, these properties were respectively 320 MPa and 0.17. Ultimately, we created a small database with 152 different structures and 304 distinct stiffness properties with the property space shown in Fig. 1B and Fig. 2B.

2.2. Structural displacement field optimization method

By performing finite element modeling of the structure, the displacements at each node within the design domain can be calculated and represented as $\overrightarrow{\boldsymbol{u}_i}$. If the target displacement field is denoted as $\overrightarrow{\boldsymbol{u}_{0,i}}$, then the optimization process can be expressed by the formula:

$$\min_{x} \boldsymbol{F} = \frac{\|(\boldsymbol{u}-\boldsymbol{u}_0)\|_2^2}{\|\boldsymbol{u}_0\|_2^2}$$

$$s.t. \boldsymbol{K}(\boldsymbol{X})\boldsymbol{u} = \boldsymbol{f}$$

$$0 \le \boldsymbol{x}_i \le 304 \tag{1}$$

where $\boldsymbol{u}$ and $\boldsymbol{f}$ are the displacement and load vectors, respectively, and $\boldsymbol{K}$ is the global stiffness matrix depending on the $\boldsymbol{x}_i$ of sub-domain. When $\overrightarrow{\boldsymbol{u}_{0,i}}$ represents the displacement field of the initial homogeneous structure, $\boldsymbol{F}$ denotes the distortion relative to the initial homogeneous displacement field, which represents the optimization process of the mechanical-cloaked structure. By removing $\overrightarrow{\boldsymbol{u}_{0,i}}$ from both the numerator and denominator, the optimization objective represents the minimized displacement field, representing the optimization process of the mechanical-sheltered structure. Additionally, $\overrightarrow{\boldsymbol{u}_{0,i}}$ can be set as any displacement field to achieve infinite design patterns.

2.3. Structural stress field optimization method

The regulatory efficacy of stress field manipulation can be validated through topological optimization of design domain configurations specifically engineered to confine mechanical stresses within predetermined protected regions shown in Fig. 3A. By performing finite element modeling of the structure, the stresses at each node within the design domain can be calculated and optimized, similar to the displacement field. As the physical meaning of stress is more complex, researchers have designed various equivalent stresses for different situations. A Mohr's circle can fully describe the stress state at any point

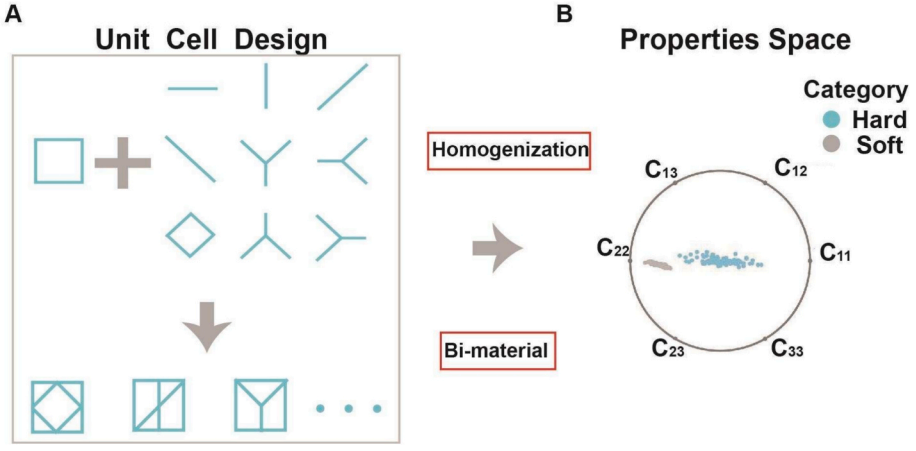

Fig. 2. Schematic diagram of the unit cell set generation. A. Method for obtaining anisotropic unit cells. B. Radar chart of the homogenized stiffness tensor after assigning two different material properties to the unit cell.

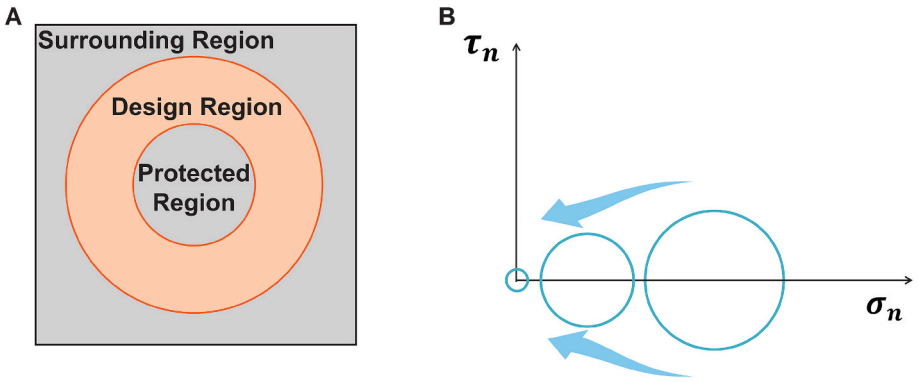

Fig. 3. A. The region definition adopted in mechanical-stress-barrier structure with designed, protected, and surrounding region. B. Optimization process of equivalent stress.

within a two-dimensional structure. As shown in Fig. 3B, the optimization process aims to reduce stress in all directions. The position and radius of Mohr's circle can be fully represented by two parameters: the average of the two principal stresses, $\sigma_0 = (\sigma_1 + \sigma_2)/2$, and the maximum shear stress, τ_{max}. Reducing these two parameters minimizes stress in all directions, and we propose the equivalent stress for this optimization process as:

$$\sigma_e = \sqrt[2]{(\sigma_0)^2 + (\tau_{\max})^2} \tag{2}$$

Since the stress within a Q4 element varies linearly, the stress at the center of each element can represent the stress for the entire element, approximating the stress field of the overall structure. Thus, the optimization process can be expressed by the formula:

$$\begin{aligned} &\min_x \boldsymbol{F} = \frac{\sum \boldsymbol{\sigma_e}}{\boldsymbol{N}} \\ &s.t. \boldsymbol{K}(X)\boldsymbol{u} = \boldsymbol{f} \\ &0 \le \boldsymbol{x_i} \le 304 \end{aligned} \tag{3}$$

where $\boldsymbol{N}$ represents the number of elements within the design domain, and the objective function $\boldsymbol{F}$ represents the average equivalent stress in the protected region.

3. Simulation and experiment for a mechanical cloak

To validate our design framework, metamaterials with a circular void were examined. Specifically, for the whole original design domain

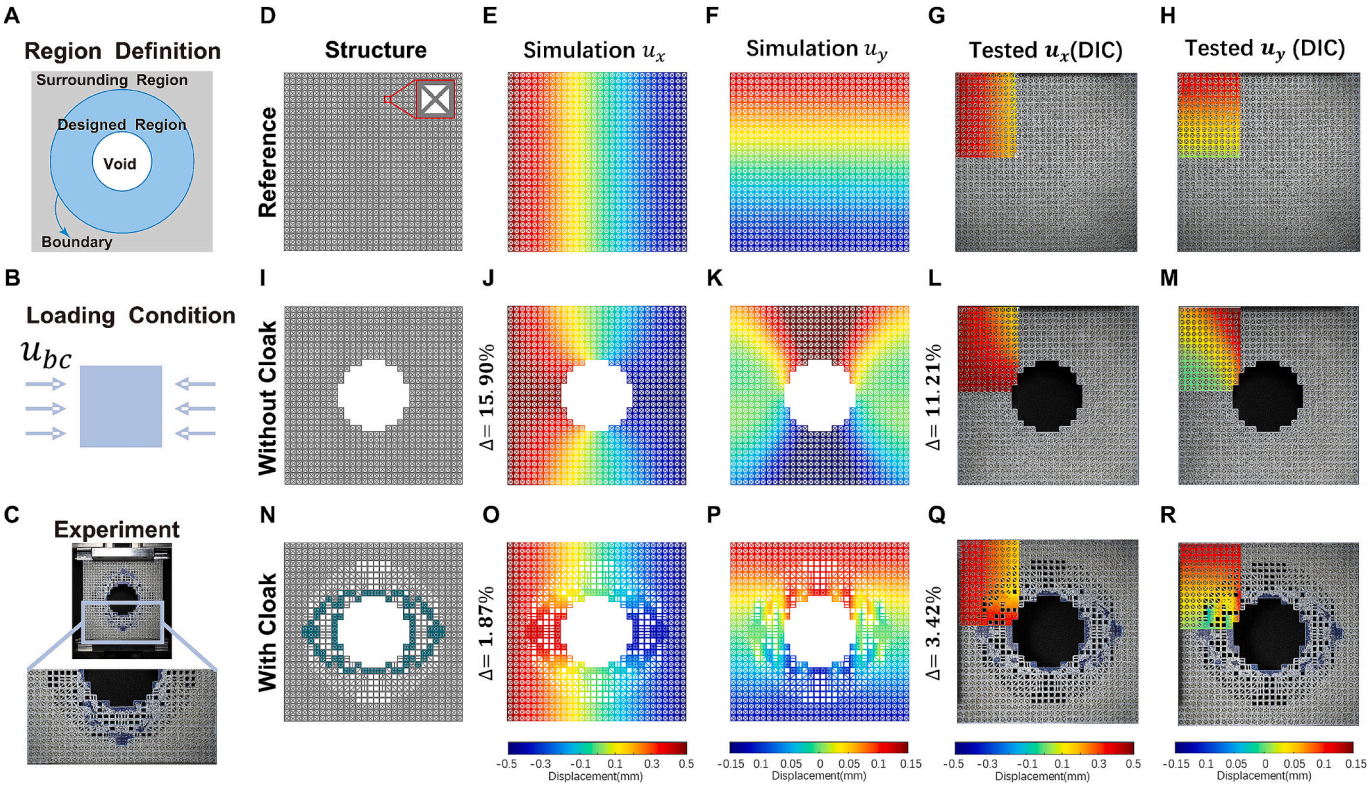

Fig. 4. (A) Definition of the designing region; (B) Displacement loading conditions applied; (C) Experimental setup for displacement field measurements and the close view of the structure. Comparison of the numerical and experimental displacement fields obtained for the reference (D–H), voided without a cloak (I–M), and cloaked (N–R) structure.

with existing voids or defects, the area around the voids was defined as the designing region Ω_c for clock function (Fig. 4A), where displacement was manipulated through the microstructure design in this region, so that the displacement field in the surrounding region Ω_s was preserved as if the voids were not present. Consequently, for an observer located at any point within Ω_s, these voids were "mechanically invisible", including both the boundaries and the interior. To facilitate the loading condition in the experimental apparatus, a displacement boundary condition of $u_{bc} = 0.5$ mm (0.67 % average strain) was applied to the left and right sides of the original design domain, while the top and bottom boundaries were kept free with no constraints, as shown in Fig. 4B. We refer to this configuration as a "displacement-free" boundary condition, termed as U_f. Note that the loading remained within the elastostatic regime throughout the process. The generated metamaterials with optimized microstructures were printed and then tested, as shown in Fig. 4C (see Appendix for more details). To facilitate displacement tracking in experimental measurement, a simple four-rod cubic lattice was chosen as the base cell (shown in Fig. 4D, Inset). For those without any voids as reference, the nodal displacement was recorded as u_0. Subsequently, simulations and experiments were performed on metamaterials with and without the designed domain Ω_c compared with the reference. The nodal displacements in the surrounding region were recorded as u_i. To evaluate the effectiveness of the proposed method in mitigating the effects of internal voids, the degree of displacement field distortion was quantified using a relative displacement difference formula Δ, given by:

$$\Delta = \frac{\sqrt{\sum_{\Omega_s}(\overrightarrow{\boldsymbol{u_i}} - \overrightarrow{\boldsymbol{u_0}})^2}}{\sqrt{\sum_{\Omega_s}(\overrightarrow{\boldsymbol{u_0}})^2}} \tag{4}$$

Ideally, the distortion of the displacement field Δ should be zero, indicating that the displacements at each point u_i were identical to those in the uniform structure u_0. Therefore, this was set as the optimization objective, as described in more detail in the Appendix.

The simulated and tested displacement fields were compared for those metamaterials with a cloak, without cloak design and the reference ones, as illustrated in Fig. 4D-R. By simulation, for the reference metamaterials without voids, a uniform transition was exhibited from one end to the other along both *x* and *y* directions (Fig. 4E-F). For those without a cloak, as voids were introduced, the overall stiffness decreased. At the same time, the internal load transmission paths changed, leading to an increased displacement near the voids (Fig. 4J-K), where the distortion Δ reached 15.9 %. For the optimized metamaterials with a cloak, the generated unit cells were arranged periodically, resulting in a specified pattern shown in Fig. 4N. Generally, the stiffer green elements naturally clustered to form a ring around the voids, compensating for the stiffness loss of voids; whereas in directions where the displacement field was prone to distortion, the softer gray unit cells tend to align towards stiffer ones to optimize the transmission path. This optimized configuration enhanced the structural loading capacity, diminishing the displacement field distortion caused by the voids. The simulated results (Fig. 4O-2P) showed a largely restored uniform displacement field in the surrounding regions like the original structure, with the distortion parameter reduced to 1.87 % (from 15.9 % of the above-mentioned metamaterials without a cloak). To further validate these findings, the reference structure (Fig. 4G-H), the voided structure (Fig. 4L-M), and the cloaked structure (Fig. 4Q-R) were additively manufactured and then tested. Considering structural symmetry, displacements from the upper left corner of each structure were measured. Generally, the experimental displacements matched well the simulated ones in terms of both displacement distribution and displacement distortion (reduced from 11.21 % in the voided structure to 3.42 % in the cloaked structure).

To demonstrate the effectiveness and universality of the design framework proposed in this study, heterogeneous metamaterials with parent materials of different ratios of Young's moduli of ~2, defined as λ under various boundary loading conditions, were examined (Movie S1 for $\lambda = 10$). Based on the modulus distribution for the same class of materials [46], λ values of 10, 30, 60, and 90 were, respectively, selected for optimization. Under displacement boundary conditions, those with two different Young's modulus ratios exhibited similar patterns, as shown in Fig. 5A. The distortion parameters for the two cases were also comparable, respectively, with values of 1.87 % ($\lambda = 10$) and 1.77 % ($\lambda = 30$), as indicated in Fig. 5E. Under the force boundary conditions shown in Fig. 5B-5C, referred to as the "pressure-free" condition (Pf) and "dilating" boundary condition, the distortion parameters for the voided structures respectively reached 111.5 % and 125.84 % (Fig. 5E). A constant compressive pressure of $p_{bc} = 70.40$ k Pa was applied to keep the average strain ~1 % and ensure that the structure remained in the linear elastic deformation range. However, for cloaked structures, the optimization results for those with two different Young's modulus ratios revealed that stiffer (green) elements formed a ring within the design domain to compensate for the stiffness loss due to the voids. This optimized pattern enabled the structure to resist constant force boundary conditions, reducing the displacement field distortion. Under shear boundary conditions (Fig. 5D), similar patterns were obtained for those with two different material Young's modulus ratios, with the distortion Δ reduced from 30.37 % to 0.35 % ($\lambda = 10$) and 0.45 % ($\lambda = 30$), nearly eliminating the displacement field distortion. Similar patterns were obtained for metamaterials with $\lambda = 60$ and $\lambda = 90$; the detailed microstructures and corresponding displacement fields are illustrated in Figs. S1-S4 with further details in the Appendix. The four selected stiffness ratios cover the typical range of Young's modulus found in common engineering materials shown in Fig. S5 [47]. As the stiffness contrast increases, the structures exhibit improved cloaking performance under the Pf boundary condition, while a slight reduction in cloaking effectiveness is observed under the dilating boundary condition. Under the other two boundary conditions, the performance remains relatively stable. Overall, all cases demonstrate good cloaking capability.

In contrast to data-driven design approaches that rely on a large number of microstructures [24], this study expands the range of stiffness tensor properties of the candidate unit set by employing two constituent materials. As a result, improved performance in static elastic cloaking was achieved, particularly under force boundary conditions, where significant enhancement was observed. Moreover, instead of first optimizing the internal stiffness distribution and then mapping it to corresponding unit cells, our approach directly optimizes the selection of unit cells, thereby establishing a more direct correspondence between the optimized result and the physical structure. Compared with previous data-driven design approaches where only one single material was utilized, no matter how complex the generated unit cells were, the distortion Δ was greater, and the resulting metamaterials could not fully compensate for the decrease in load-bearing capacity. Accordingly, those with two material systems in our study demonstrated significant advantages. Also, the void shape could be arbitrarily specified, with the cloak shapes (cloak region Ω_c) additionally optimized, as shown in Fig. S6.

4. Physical field manipulation

4.1. Displacement field manipulation

Based on these studies, the key point for realizing mechanical cloaking lies in regulating nodal displacements of unit cells. This design method by manipulating the overall displacement field was further expanded for other functionality using three simulation examples (Movie S2).

Facial expression changes. A cartoon face structure was defined in Fig. 6A. Our goal was to change the facial expression by displacement field control. By controlling the displacement away from the center

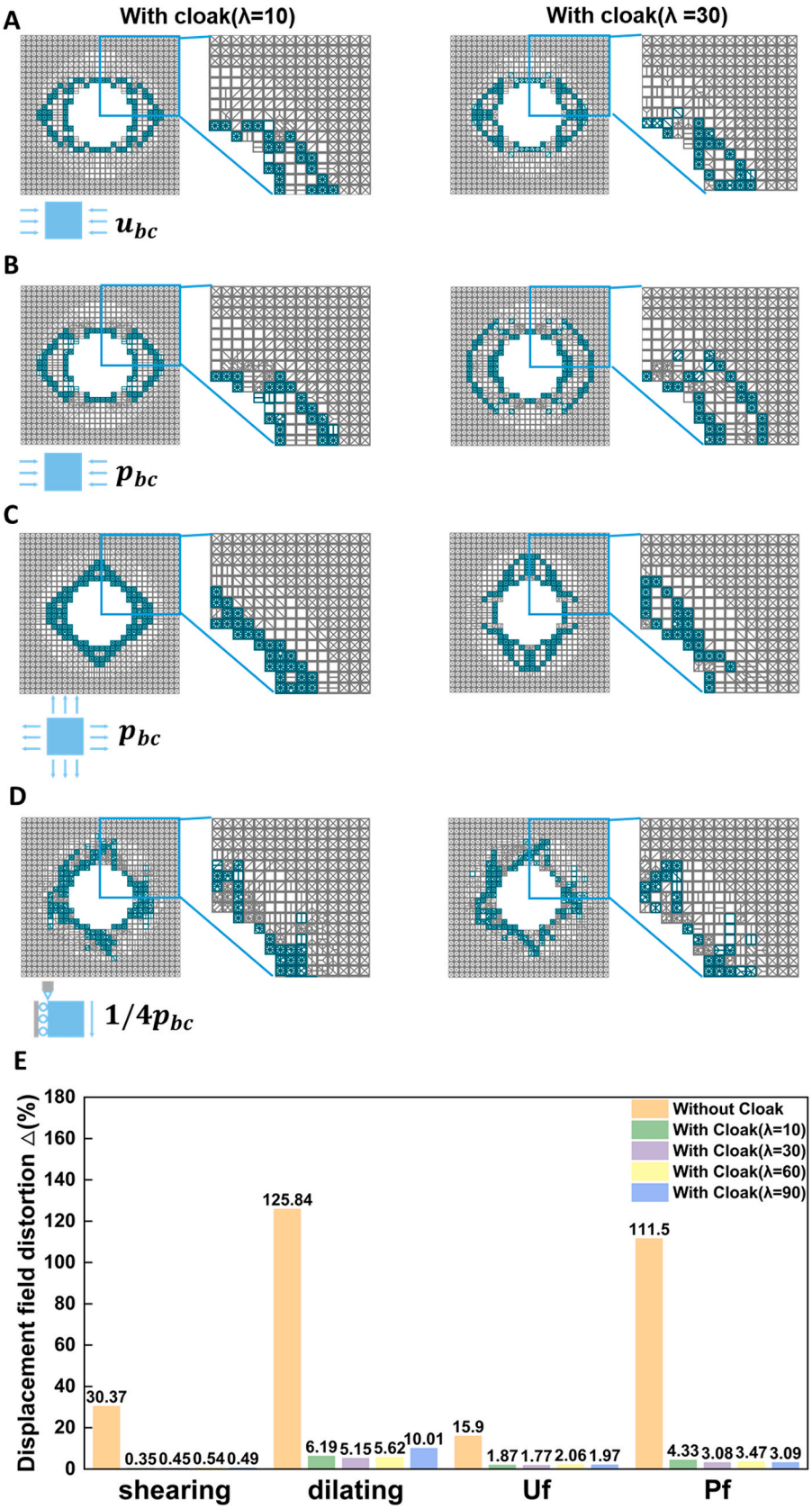

Fig. 5. Design results for different boundary conditions and material Young's modulus ratios. (A–D) Cloaked structures under (A) displacement boundary condition, (B) pressure boundary condition, (C) dilating boundary condition, and (D) shearing boundary condition. (E) Bar graph for the relative displacement differences of different boundary conditions and material Young's modulus ratios.

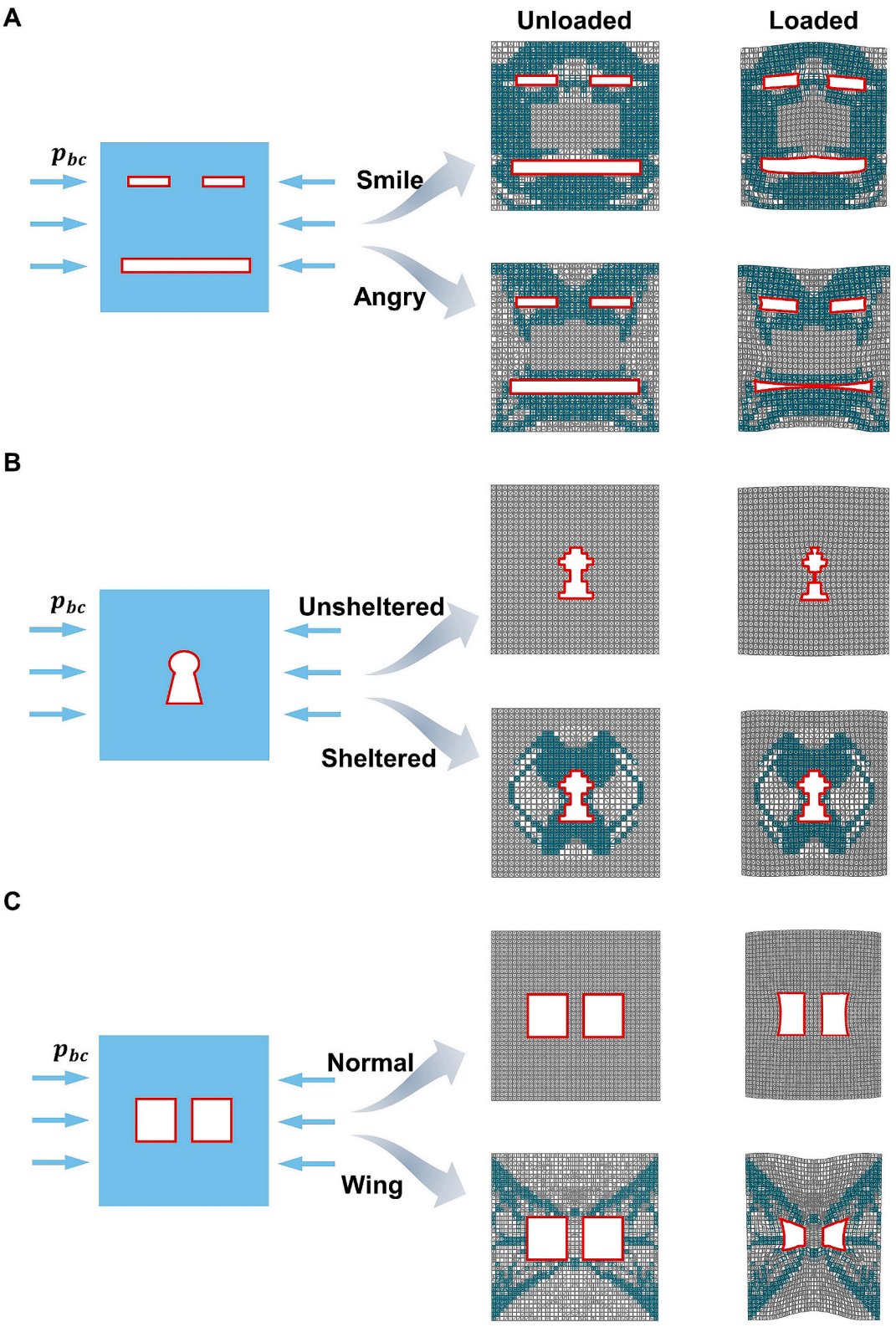

Fig. 6. Design results of the heterogeneous mechanical metamaterials for different application scenarios. (A) Customized cartoon facial expressions. (B) Mechanical shelter and (C) Wing-shaped voids, compared with the initial homogeneous structure.

(details are given in the Appendix), the optimized structure was shown as the unloaded structure with a specified pattern (Fig. 6A). After loading, the facial structure produced a "smile" expression (facial eyes move outward) by simulation. Alternatively, by concentrating the displacement towards the center, the facial expression transformed into an "angry" expression.

Mechanical shelter. A key-patterned void shape was specified and a design area around it was defined for optimization. The displacement summation value along the void edge was taken as the optimization objective to minimize the shape change of the void to nearly zero (as

detailed in the Appendix). After optimization, the displacement value at the void edge was significantly reduced to only 0.0181 % of the original value, and the shape change was nearly undetectable. The exhibiting characteristic could isolate the external physical field from being detected by those inside the voids, *i.e.*, behaving as a mechanical shelter. For example, for embedded chips or sensors, the optimized structure would protect their structural integrity and function from external disturbances.

Shape controlling. To arbitrarily control the local shape remained a challenge. Here, an example was illustrated by governing two rectangular voids to a "wing-like" shape (Fig. 6C). The optimization was carried out by manipulating the local displacement as the objective. The behavior of the optimized structures transformed from those with positive Poisson's ratio to a negative ratio. Interestingly, in the optimized structure, stiffer units were arranged in a pattern resembling a "butterfly", which again highlighted the advantage of incorporating dual-material systems in the design framework. The framework enabled other atypical mechanical behaviors, such as local displacement field rotation (Fig. S7). The deformation process is shown by simulation in Movie S2.

4.2. Stress field manipulation

Batteries and sensors are used more widely in smart vehicles, which may suffer damage or impact loading in real applications. To protect their functionality, one objective to markedly reduce the stress on these functional components is through a region that encloses them. The stress at any point within a two-dimensional structure can be represented by a Mohr's circle, which describes the stress-state through the parameters of the circle, specifically its center position and radius. From this perspective, we proposed an equivalent stress σ_e that can serve as an optimization objective to reduce stress in all directions. A homogeneous unit cell representing the functional component (protected region) was utilized shown in Fig. 3A. The average equivalent stress $\overline{\sigma_e}$ in the protected region was then taken as the optimization objective. Fig. 7A shows the optimization results under a constant force applied to the left and right sides. On the left and right sides, "arrow-like" parts formed by stiffer materials were observed with clear directionality, which directed the stress to be transmitted toward the top and bottom regions with stiffer sections.

This structure generated a stress barrier around functional components, reducing $\overline{\sigma_e}$ from 100 % (original value) to 16.12 %. Notably, with limited volume, the barrier region could be increased as the radius of the protected region is reduced, such that $\overline{\sigma_e}$ would approach zero. To demonstrate that this optimization process minimizes the stress in the protected region, we repeated the optimization process by gradually reducing the radius of the protected region shown in Fig. 3A, thereby increasing the design area. We defined the ratio of the average equivalent stress after optimization to the average equivalent stress before optimization in the protected region as "Decrease." As shown in Fig. S8, the equivalent stress approached zero as the radius gradually decreased. Theoretically, as the design domain increases, a region completely unaffected by external stress will be achieved, with the mechanical stress barrier completely shielding the external stress. This suggests that, if the

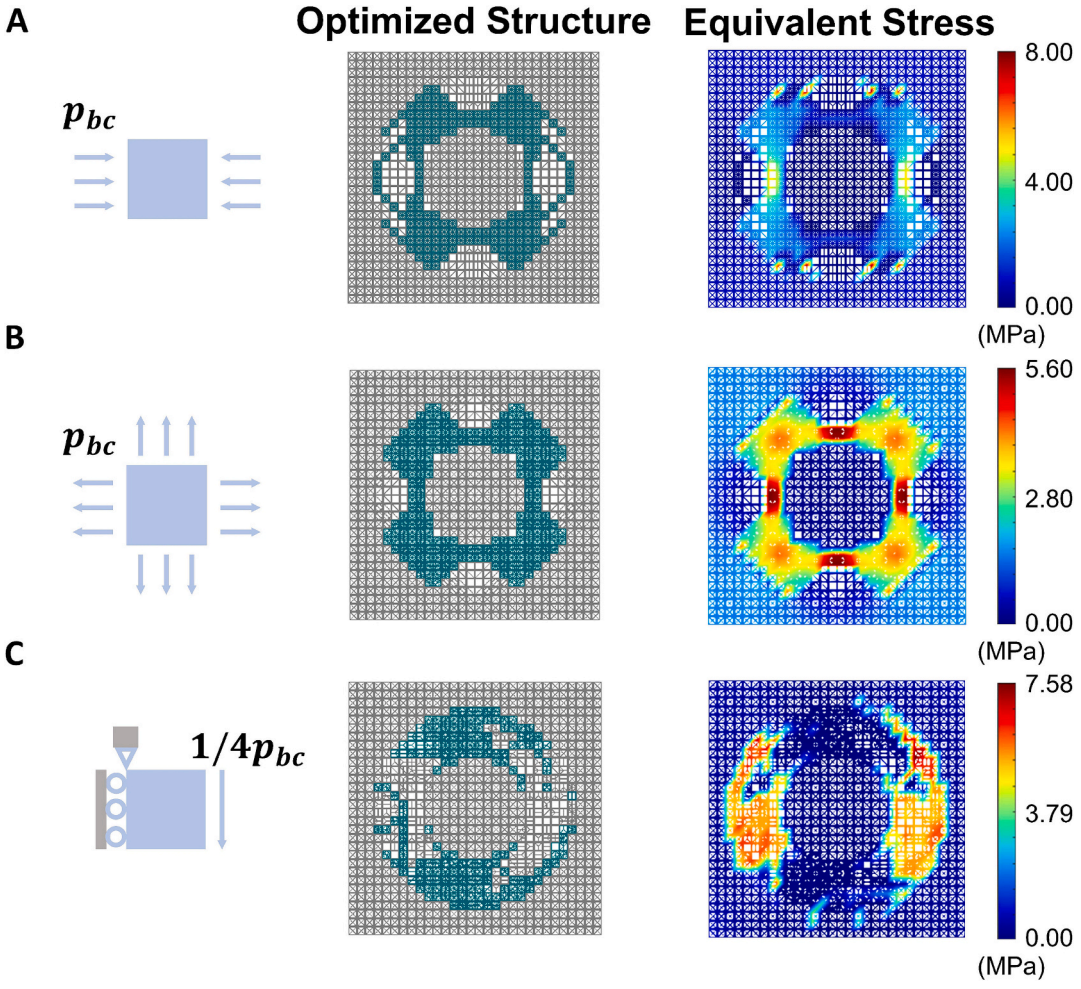

Fig. 7. Optimization results of stress barriers and their corresponding equivalent stress field distributions under different boundary conditions: under (A) pressure boundary condition, (B) dilating boundary condition, and (C) shear boundary condition.

stress barrier was large enough, a completely protected region could be created within the structure where no stress was transmitted, ensuring absolute safety and reliability for the functional components in this area. The internal stress contours are shown in Figs. S9-S10, which further validates the effectiveness of using Mohr's circle parameters as the optimization objective.

The generated structures under dilating boundary conditions are shown in Fig. 7B, where stiffer material formed a ring surrounding the protected area with four thickened corners; this reduces $\overline{\sigma_e}$ from 100 % (original value) to 20.09 %. The optimization results under shear boundary conditions are shown in Fig. 7C. The stress barrier causes a higher concentration of stress on both sides, which reduces $\overline{\sigma_e}$ to 47.12 %. The stress reduction, however, was not significant, indicating that a larger stress barrier was necessary under such loading conditions to fully attenuate the stress within the barrier. This simulation of the stress barrier structure under different loading conditions is shown in Movie S3.

5. Conclusion

A universal design framework for heterogeneous mechanical metamaterials with various functionalities has been established. By employing a Nature-inspired multi-material with irregular features, unit cells with simple struts were constructed with two different parent materials as microstructure databases. The spatial distribution of a limited set of unit cells was optimized, and irregular and multi-material metamaterials were obtained for various functions. The optimized *meta*-structures for mechanical cloak performance were 3D printed and tested. The measured displacement field distribution agreed well with the simulated distribution, which demonstrated the effectiveness of the design approach. Microstructures with various Young's modulus ratios of two parent materials were examined, with the created metamaterials exhibiting similar cloaking effects under various loading conditions, demonstrating the design approach was effective irrespective of the type of materials that were used. In addition to the establishment of a mechanical cloak, other functionalities were realized through the manipulation of physical fields. Atypical mechanical behavior, such as facial expression change, mechanical shelter, shape control and local displacement field rotation, were generated by governing the displacement field. Additionally, by manipulating the stress field, the stress could be decreased for protection when the equivalent stress was set as the optimization target. For engineering applications, this framework can quickly initiate analysis, regardless of the complexity of the scenario. This approach enables heuristic solutions to functional structural design, significantly reducing labor-intensive modeling and experimental costs.

CRediT authorship contribution statement

Zhuo Chen: Writing – original draft, Validation, Software, Methodology, Investigation, Conceptualization. **Huitian Wang:** Visualization, Software, Methodology. **Zihan Hu:** Validation. **Limin Zhou:** Writing – review & editing. **Yiu Wing Mai:** Writing – review & editing. **Robert O. Ritchie:** Writing – review & editing. **Sha Yin:** Writing – review & editing, Supervision, Resources, Methodology, Funding acquisition.

Declaration of competing interest

The authors declare that they have no known competing financial interests or personal relationships that could have appeared to influence the work reported in this paper.

Acknowledgments

This research is supported by National Natural Science Foundation of China (Nos. 12172025, 12322204), and the National Key Research and Development Program of China (2023YFB2504600).

Appendix A. Supplementary data

Supplementary data to this article can be found online at https://doi.org/10.1016/j.matdes.2025.114467.

Data availability

The database and code that support the findings of this study are available at https://doi.org/10.6084/m9.figshare.28529123.v1.

References

[1] J. Gao, et al., Rational designs of mechanical metamaterials: formulations, architectures, tessellations and prospects, Mat. Sci. Eng. R 156 (2023) 100755, https://doi.org/10.1016/j.mser.2023.100755.
[2] Y. Chen, Y.W. Mai, L. Ye, Perspectives for multiphase mechanical metamaterials, Mat. Sci. Eng. R 153 (2023) 100725, https://doi.org/10.1016/j.mser.2023.100725.
[3] J. Bauer, et al., Nanolattices: an emerging class of mechanical metamaterials, Adv. Mater. 29 (2017) 1701850, https://doi.org/10.1002/adma.201701850.
[4] X.L. Yu, J. Zhou, H.Y. Liang, Z.Y. Jiang, L.L. Wu, Mechanical metamaterials associated with stiffness, rigidity and compressibility: a brief review, Prog. Mater Sci. 94 (2018) 114–173, https://doi.org/10.1016/j.pmatsci.2017.12.003.
[5] H. Yasuda, L.M. Korpas, J.R. Raney, Transition waves and formation of domain walls in multistable mechanical metamaterials, Phys. Rev. Appl 13 (2020) 054067, https://doi.org/10.1103/PhysRevApplied.13.054067.
[6] P.C. Jiao, J. Mueller, J.R. Raney, X.Y. Zheng, A.H. Alavi, Mechanical metamaterials and beyond, Nat. Commun. 14 (2023) 6004, https://doi.org/10.1038/s41467-023-41679-8.
[7] K. Liang, et al., Ideal energy-absorbing metamaterials based on self-locking bistable structures, Mater. Horiz. 12 (2025) 4165–4176, https://doi.org/10.1039/D5MH00502G.
[8] D.C. Da, Y.C. Chan, L.W. Wang, W. Chen, Data-driven and topological design of structural metamaterials for fracture resistance, Extreme Mech. Lett. 50 (2022) 101528, https://doi.org/10.1016/j.eml.2021.101528.
[9] Y. Jia, K. Liu, X.S. Zhang, Modulate stress distribution with bio-inspired irregular architected materials towards optimal tissue support, Nat. Commun. 15 (2024) 4072, https://doi.org/10.1038/s41467-024-47831-2.
[10] Y. Huang, W.H. Guo, J. Jia, L.B. Wang, S. Yin, Novel lightweight and protective battery system based on mechanical metamaterials, Acta Mech. Solida Sin. 34 (2021) 862–871, https://doi.org/10.1007/s10338-021-00249-5.
[11] Z. Vangelatos *et al.*, Strength through defects: a novel Bayesian approach for the optimization of architected materials. *Sci. Adv.* **7**, eabk2218(2021). https://doi.org/10.1126/sciadv.abk2218.
[12] Y. Tian, H.T. Wang, Z. Chen, Q. Wu, S. Yin, Design principles for dual-phase lattice cylindrical tubes with excellent energy absorption capability, Compos. Struct. 359 (2025) 119015, https://doi.org/10.1016/j.compstruct.2025.119015.
[13] H.T. Wang, J.J. You, Y. Tian, Z. Chen, S.Y. Yin, Dynamic mechanical behavior of sinusoidal corrugated dual-phase lattice metamaterials by additive manufacturing, Exp. Mech. Mech. AM (2025), https://doi.org/10.1007/s11340-025-01160-7.
[14] T. Bückmann, M. Kadic, R. Schittny, M. Wegener, Mechanical cloak design by direct lattice transformation, Proc. Natl. Acad. Sci. U.S.A. 112 (2015) 4930–4934, https://doi.org/10.1073/pnas.1501240112.
[15] L.Y. Hai, Q. Zhao, Y.G. Meng, Unfeelable mechanical cloak based on proportional parameter transform in bimode structures, Adv. Funct. Mater. 28 (2018) 1801473, https://doi.org/10.1002/adfm.201801473.
[16] M. Kadic, et al., Elastodynamic behavior of mechanical cloaks designed by direct lattice transformations, Wave Motion 92 (2020) 102419, https://doi.org/10.1016/j.wavemoti.2019.102419.
[17] D.R. Reid, et al., Auxetic metamaterials from disordered networks, Proc. Natl. Acad. Sci. U.S.A. 115 (2018) E1384–E1390, https://doi.org/10.1073/pnas.1717442115.
[18] M.J. Mirzaali, H. Pahlavani, A.A. Zadpoor, Auxeticity and stiffness of random networks: lessons for the rational design of 3D printed mechanical metamaterials, Appl. Phys. Lett. 115 (2019) 021901, https://doi.org/10.1063/1.5096590.
[19] C.M. Portela, et al., Extreme mechanical resilience of self-assembled nanolabyrinthine materials, Proc. Natl. Acad. Sci. U.S.A. 117 (2020) 5686–5693, https://doi.org/10.1073/pnas.1916817117.
[20] S. Kumar, S.H. Tan, L. Zheng, D.M. Kochmann, Inverse-designed spinodoid metamaterials, Npj Comput. Mater. 6 (2020) 73, https://doi.org/10.1038/s41524-020-0341-6.
[21] L. Zheng, S. Kumar, D.M. Kochmann, Data-driven topology optimization of spinoidal metamaterials with seamlessly tunable anisotropy, Comput Method Appl M 383 (2021) 113894, https://doi.org/10.1016/j.cma.2021.113894.
[22] K. Liu, R. Sun, C. Daraio, Growth rules for irregular architected materials with programmable properties, Science 377 (2022) 975–981, https://doi.org/10.1126/science.abn1459.

[23] Y.Q. Jia, K. Liu, X.S. Zhang, Unstructured growth of irregular architectures for optimized metastructures, J. Mech. Phys. Solids 192 (2024) 105787, https://doi.org/10.1016/j.jmps.2024.105787.
[24] L.W. Wang, et al., Mechanical cloak via data-driven aperiodic metamaterial design, Proc. Natl. Acad. Sci. U.S.A. 119 (2022) e2122185119, https://doi.org/10.1073/pnas.2122185119.
[25] J.H. Bastek, S. Kumar, B. Telgen, R.N. Glaesener, D.M. Kochmann, Inverting the structure-property map of truss metamaterials by deep learning, Proc. Natl. Acad. Sci. U. S. A. 119 (2022) e2111505119, https://doi.org/10.1073/pnas.2111505119.
[26] J. Boddapati, C. Daraio, Planar structured materials with extreme elastic anisotropy. *Mater. Des.* **246**, 113348(2024). Planar structured materials with extreme elastic anisotropy.
[27] W. Zhang, S. Yin, T.X. Yu, J. Xu, Crushing resistance and energy absorption of pomelo peel inspired hierarchical honeycomb, Int. J. Impact Eng 125 (2019) 163–172, https://doi.org/10.1016/j.ijimpeng.2018.11.014.
[28] U.G.K. Wegst, H. Bai, E. Saiz, A.P. Tomsia, R.O. Ritchie, Bioinspired structural materials, Nat. Mater. 14 (2015) 23–36, https://doi.org/10.1038/nmat4089.
[29] K. Madi, et al., In situ characterization of nanoscale strains in loaded whole joints via synchrotron X-ray tomography, Nat. Biomed. Eng. 4 (2020) 343–354, https://doi.org/10.1038/s41551-019-0477-1.
[30] W. Yang, G.P. Zhang, H.S. Liu, X.W. Li, Microstructural characterization and hardness behavior of a biological shell, J. Mater. Sci. Technol. 27 (2011) 139–146, https://doi.org/10.1016/S1005-0302(11)60039-X.
[31] M. Eder, S. Amini, P. Fratzl, Biological composites-complex structures for functional diversity, Science 362 (2018) 543–547, https://doi.org/10.1126/science.aat8297.
[32] M.A. Meyers, J. McKittrick, P.Y. Chen, Structural biological materials: critical mechanics-materials connections, Science 339 (2013) 773–779, https://doi.org/10.1126/science.1220854.
[33] Y. Nian, et al., Nature-inspired 3D printing-based double-graded aerospace negative Poisson's ratio metastructure: design, fabrication, investigation, optimization, Compos. Struct. 348 (2024) 118482, https://doi.org/10.1016/j.compstruct.2024.118482.
[34] S. Yin, H.T. Wang, J.N. Li, R.O. Ritchie, J. Xu, Light but tough bio-inherited materials: Luffa sponge based nickel-plated composites, J Mech Behav Biomed 94 (2019) 10–18, https://doi.org/10.1016/j.jmbbm.2019.02.029.
[35] S. Yin, et al., Tough nature-inspired helicoidal composites with printing-induced voids, Cell Rep. Phys. Sci. 1 (2020) 100109, https://doi.org/10.1016/j.xcrp.2020.100109.
[36] J.T. Li, et al., Spider silk-inspired artificial fibers, Adv. Sci. 9 (2022) 2103965, https://doi.org/10.1002/advs.202103965.
[37] H. Rhee, et al., A study on the structure and mechanical behavior of the carapace: a pathway to design bio-inspired synthetic composites, Mat. Sci. Eng. C-Mater. 29 (2009) 2333–2339, https://doi.org/10.1016/j.msec.2009.06.002.
[38] A.R. Mao, N.F. Zhao, Y.H. Liang, H. Bai, Mechanically efficient cellular materials inspired by cuttlebone, Adv. Mater. 33 (2021) 2007348, https://doi.org/10.1002/adma.202007348.
[39] G.D. Bixler, B. Bhushan, Fluid drag reduction with shark-skin riblet inspired microstructured surfaces, Adv. Funct. Mater. 23 (2013) 4507–4528, https://doi.org/10.1002/adfm.201203683.
[40] B. Dean, B. Bhushan, Shark-skin surfaces for fluid-drag reduction in turbulent flow: a review, Philos T R Soc A 368 (2010) 4775–4806, https://doi.org/10.1098/rsta.2010.0201.
[41] M.J. Mirzaali, et al., Mechanics of bioinspired functionally graded soft-hard composites made by multi-material 3D printing, Compos. Struct. 237 (2020) 111867, https://doi.org/10.1016/j.compstruct.2020.111867.
[42] M. He, et al., Multi-material topology optimization of piezoelectric composite structures for energy harvesting, Compos. Struct. 265 (2021) 113783, https://doi.org/10.1016/j.compstruct.2021.113783.
[43] D.F. Wang, S.H. Li, Material selection decision-making method for multi-material lightweight automotive body driven by performance, P I Mech Eng L-J Mat 236 (2022) 730–746, https://doi.org/10.1177/14644207211055661.
[44] A. Nazir, et al., Multi-material additive manufacturing: a systematic review of design, properties, applications, challenges, and 3D printing of materials and cellular metamaterials, Mater Design 226 (2023) 111661, https://doi.org/10.1016/j.matdes.2023.111661.
[45] L. Xia, P. Breitkopf, Design of materials using topology optimization and energy-based homogenization approach in Matlab, Struct. Multidiscip. Optim. 52 (2015) 1229–1241, https://doi.org/10.1007/s00158-015-1294-0.
[46] M. F. Ashby, 2011. *Chapter 4 – Material Property Charts* in: M. F. Ashby, Materials Selection in Mechanical Design (Fourth Edition), Elsevier, pp. 57–96. https://doi.org/10.1016/B978-1-85617-663-7.00004-7.
[47] M. F. Ashby, K. Johnson, 2014. *Chapter 3 - Materiality, Design, and Creativity* in: M. F. Ashby, K. Johnson, Materials and Design (Third Edition), Elsevier, pp. 34-60. https://doi.org/10.1016/B978-0-08-098205-2.00003-2.